Microscopic Susceptibility Variation and Transverse Relaxation: Theory and Experiment

Robert M. Weisskoff, Chun S. Zuo, Jerrold L. Boxerman, Bruce R. Rosen

Microscopic susceptibility variations invariably increase apparent transverse relaxation rates. In this paper, we present comparisons between Monte Carlo simulations and experiments with polystyrene microspheres to demonstrate that this enhanced relaxation can be explained quantitatively for both spin echo and gradient echo imaging experiments. The spheres used (1 to 30 μ), and degree of susceptibility variation (caused by 0–12 mM Dy-DTPA) covered a wide range of biologically relevant compartment sizes and contrast agent concentrations. These results show that several regimes of behavior exist, and that contrast dependence is quite different in these regimes. For a given susceptibility, $\Delta\chi$, a small range of particle sizes show peak transverse relaxation. For the range of susceptibilities found in the first pass of a clinical IV contrast agent bolus, this size range is 5 to 10 μ, or roughly capillary sized compartments. In both our simulations and experiments, smaller spheres showed quadratic relaxation versus concentration curves, and larger particles showed sublinear behavior. For particles corresponding to the peak relaxivity, the relaxation-concentration curves were linear. In addition, we demonstrated that increasing the diffusion coefficient can increase, decrease, or, paradoxically, leave unaffected the apparent relaxation rate. The regime for which the diffusion coefficient is relatively unimportant corresponds to the region of peak relaxivity. By using the Bloch-Torrey equation to produce scaling rules, the specific Monte Carlo simulations were extended to more general cases. We use these scaling rules to demonstrate why we often find that susceptibility-induced relaxation rates vary approximately linearly with concentration of injected agent.

Key words: contrast agents; susceptibility; T_2^*; Monte Carlo modeling.

INTRODUCTION

This paper summarizes our recent efforts to understand and quantify susceptibility-based NMR image contrast, and apply these results to dynamic imaging with and without contrast agents in order to quantify tissue hemodynamics, especially in the brain. These techniques, using contrast agents, have been used to measure a variety of physiological phenomena, including hypercapnia in animals (1, 2), cerebral hemodynamics in the pathological brain (3–5), and functional activation in humans (6). At lower susceptibility, these effects are also thought to be critically important in functional activation studies in the absence of contrast agents (7–12). In this paper, we will present results from simulations and experiments that demonstrate that, at least *in vitro*, we can fully explain these phenomena under conditions that resemble those *in vivo*.

The use of injectable tracers has a long history in medicine (13–17). More recently, with the advent of the tomographic modalities, these principles of tracer kinetics have been extended to positron emission tomography (PET) (18, 19) and contrast-enhanced cine CT (20–22). PET, in particular, can be made sensitive to a wide range of physiological processes, and measurements of blood flow (labeled water), blood volume (labeled hemoglobin), metabolism (FDG), etc., are beginning to become more common in clinical practice (23).

Following a contrast agent injection, tracer kinetic analysis of contrast concentration-time data can yield both flow and volume information (e.g., (24)). To measure cerebral blood volume (CBV) or cerebral blood flow (CBF) by MR, changes in signal intensity versus time first must be converted into contrast agent/tissue concentration-time curves. It is both a potential strength, as well as possible limitation, that the analogy between MR and other imaging modalities is not exact. One strength of NMR is the rich interaction of physical, chemical, and biological mechanisms that combine to produce image contrast. This paper seeks to demonstrate that while the end results of this interaction may appear complex, the complexity is both explainable and, potentially, quite useful.

The effect of spin diffusion in a uniform gradient was described in depth in Hahn's original spin echo paper (25). Torrey (26) generalized the average signal loss in a more analytically tractable method by adding a diffusion term to the Bloch equations. Other generalizations, to restricted diffusion (27) and, by analogy, diffusion in a periodic potential (28) were also presented in the pre-MRI literature. However, recent work in the MRI literature (29–32) has included several methodologies whose results, ultimately, are contradictory. For example, Gillis and Koenig (29) predicts decreased T_2 contrast with increasing proton diffusion, while Bendel (30) predicts the opposite. Even the fundamentals of the mechanisms seem unresolved. For example, one mechanism outlined

by Bauer and Schulten (32) requires capillary water permeability while a second does not. By contrast, numerical solutions (33–35) have been consistent, though to date have not been extensively verified, and are intrinsically difficult to generalize.

Our primary interest is explaining the effects of magnetically compartmentalized contrast agent. This includes both magnetic particulates as well as lanthanide chelates and deoxygenated red cells compartmentalized in the vasculature. Because a physical phantom simulating the tangled microvasculature that is faithful to the dimensions of the capillary bed is difficult to achieve, we have, in this paper, approached the "verification" of theory and experiment directly in a related case. In particular, we have performed Monte Carlo simulations for spherically shaped perturbers and demonstrated that these results are correct in physical phantoms. Although these results may not identically transfer to cylindrical capillaries filled with red blood cells, many of the results and the methods are quite general.

In this paper, we combine numerical solutions with analytic scaling rules in order to demonstrate that (1) these Monte Carlo models accurately predict measured signal loss in imaging experiments; (2) while signal loss is very compartment size dependent, effective relaxivity is approximately linear with agent concentration for capillary sized compartments; and (3) transverse relaxation enhancement for magnetic contrast agents can be very different *in vivo* than *in vitro*, and can be expected to vary based on the biodistribution of the agents.

The paper has two main parts. In the first, we compare random walk simulations to experiment for polystyrene microspheres in aqueous solution. Because the Monte Carlo simulations are simply a calculational engine, it is difficult to generalize the specific solutions to produce a clearer understanding of the susceptibility problem. In the second part of the paper, we therefore return to the Bloch-Torrey description of diffusion–for which it is difficult to obtain the specific solutions–and generate some simple equations in order to interpret our Monte Carlo results more broadly.

METHODS

Monte Carlo Calculations

General Methodology. Monte Carlo simulations of proton random walks have been used by several groups to estimate transverse relaxation enhancement caused by diffusion through inhomogeneous magnetic fields (33–35). In general, we compute a signal, S, based on the expectation of proton phases:

$$S = \langle e^{i\varphi} \rangle$$

where the expectation value is over both initial position of the protons and, for each initial position, the possible paths through the medium. While this expectation can be thought of in two pieces:

$$S(t) = \frac{1}{V} \int_v d\vec{x} \int d\varphi p(\varphi, t; \vec{x}) e^{i\varphi} \quad [1]$$

where $p(\phi, t; x)$ is the probability density function for a proton starting at position x to acquire phase ϕ by time t, the Monte Carlo methods used here combine the two integrals into a single step by accumulating the phase of N randomly distributed protons:

$$S(t) = \frac{1}{N} \sum_{n=1}^{N} e^{i\varphi_n(t)} \quad [2]$$

where $\phi_n(t)$ is the phase of the n-th proton at time t. Monte Carlo estimation is actually used twice: once explicitly to perform the expectation over starting locations; and once implicitly as the stochastic walk of the protons produces phases that must be distributed like $p(\phi; x)$.

In the spherical simulations described below, the steps to produce a Monte Carlo estimate of the change in "imaging" relaxation rate, $\Delta R2$ (defined below) were:

1. Distribute the impenetrable spherical perturbers randomly throughout a prescribed region and place a proton at the center of this universe,

2. For every time step Δt, simulate the stochastic diffusion of the proton by choosing a random displacement (with mean 0 and standard deviation $\sqrt{2D\Delta t}$, where D is the diffusion coefficient) in the x, y, and z directions,

3. Evaluate the magnetic field at the proton's new location by summing the fields of each of the perturbers, and

4. Evaluate the accumulated phase by trapezoidal integration: $\Delta\phi = \gamma B(x(t))\Delta t$. For spin echo imaging, the phase was inverted at $t = TE/2$.

Steps 2–4 were repeated, and the phase of each proton recorded, at 5-ms intervals. Steps 1–4 were repeated for N protons, typically 20,000, as discussed below.

5. Finally, the estimate for the signal was produced from the phases of the individual protons by Eq. [2] above, and all the steps, including redistributing all the perturbing particles, were repeated 10 times. In this way, an estimate for the repeatability could be determined.

We used several techniques to reduce the total time for each simulation. First, we estimated spin echo (not CPMG) and gradient echo amplitudes every 10 ms from a single time series by storing the phase evolved in each 5-ms interval and combining the phases with signs appropriate for each TE. For example, if Φ_5 represents the phase evolved in the first 5 ms, Φ_{10} the phase between 5 and 10 ms, etc., then the phase required for a spin echo at $TE = 20$ is $\Phi_5 + \Phi_{10} - \Phi_{15} - \Phi_{20}$, at $TE = 30$ is $\Phi_5 + \Phi_{10} + \Phi_{15} - \Phi_{20} - \Phi_{25} - \Phi_{30}$, while the phase for the $TE = 20$ gradient echo is $\Phi_5 + \Phi_{10} + \Phi_{15} + \Phi_{20}$.

The second time saver was that we estimated the signal loss due to many different overall susceptibility differences, $\Delta\chi$, from the same random walks/perturber combination. This is because for the systems studied, the magnetic field perturbation was, to a high accuracy, linear in $\Delta\chi$, and thus changes in $\Delta\chi$ affect the phases Φ linearly. Because nearly all of the computational time was spent in evaluating the fields from each of the spheres at each of the proton's locations during their trajectories, computing the signal loss for multiple sus-

ceptibility differences added negligible time to the total computation. (This step could add correlation between the different $\Delta\chi$'s, and could therefore bias estimates of the dependence of $\Delta R2$ on concentration. However, we found no significant differences between results computed using this technique and those for which different random walks were used for the different $\Delta\chi$'s.)

The simulation was first tested using a linear gradient field perturbation, and comparing the resulting signal versus time curves to the standard result (36), $S = \exp(-(\gamma G)^2 TE^3/12)$. Intensities agreed to better than 1%. Simulations were performed on Sun Sparc workstations as well as a Silicon Graphics 4D/480/VGX.

Simulations with Impenetrable Spheres. For the case of a spherical particle, the magnetic field perturbation takes the form (37) (in cgs units):

$$\frac{\Delta B_z(r, \theta)}{B_0} = \frac{4\pi}{3}\Delta_x\left(\frac{R}{r}\right)^3 (3\cos^2\theta - 1) \qquad [3]$$

where r and θ are the usual spherical coordinates, R is the radius of the sphere, and $\Delta\chi$ is the magnitude of the susceptibility difference between the sphere and the surrounding medium.

These spheres were distributed uniformly in the simulation universe, described in step 1 above. Unlike previous simulations (e.g., (33)), we did not assume a periodic distribution of these spheres. The size of this universe depended on the diffusion coefficient, the maximum TE, and the size of the spheres. The half length of the universe was chosen to be $\sqrt{2\,D\,TE} + 20\,R$. That is, the universe size was chosen to be roughly twice the RMS diffusion distance at the end of the simulated MR experiment plus a "buffer" region to minimize boundary effects at the edge of the protons' expected path. Because the magnetic field falls off like R^{-3}, we made this buffer region 20 sphere radii long. (At maximum $\Delta\chi$ we let the boundary vary from 5 to 50 sphere radii, and found no reproducible changes by letting this region be larger than 15. This choice may produce some inefficiency for smaller $\Delta\chi$, which might permit a smaller universe size due to smaller phase accumulation.)

We computed signal intensity versus echo time using Monte Carlo methods for sphere sizes matching experimental conditions, described below. Simulations used 20,000 protons, walking in $\Delta t = 200$ µs time steps during echo times of 10 to 100 ms (Hahn Echo). In early simulatations, the time step for the proton diffusion, Δt, was chosen to be shorter, but subsequent simulations showed no difference, even for the smallest perturber size, at $\Delta t = 200$ µs. The diffusion coefficient was set to 1.3×10^{-5} cm^2/s, which corresponded to the water diffusion coefficient for the experimental conditions, below.

The effective (monoexponential) T_2 or T_2^* was estimated by computing the inverse of the slope of the resulting log(signal) versus TE curve for each sphere size at each $\Delta\chi$. From our results, all but the largest spheres showed primarily monoexponential decay.

The difference between the volume susceptibility of the magnetic spheres and the background, $\Delta\chi$, was varied between 0 and 0.6×10^{-6} cgs units, which is equivalent to the susceptibility variation relative to water caused by

a solution of roughly 20 mM Gd-DTPA or the 12 mM Dy-DTPA used in the experiments below.

Experiments with Spheres

Preparation of Samples. Precision polystyrene microspheres (Bang Laboratory, Carmel, IN) of various diameters, ranging from 0.1 to 30 µm, size standard deviation <5%, were used. Samples were prepared as 2% volume fraction of aqueous solutions of polystyrene microspheres/0.05% Triton X-100 (a surfactant). As prepared, the particles remained in solution without noticeable precipitation during the image acquisition time.

We modified the susceptibility difference between the microspheres and the solvent by adding Dysprosium diethylene triaminepentaacetic acid (Dy-DTPA)$^{2-}$, prepared by standard method. For impenetrable spheres, the magnetic field deviations are identical if we change either the susceptibility of the spheres or of the solvent. The concentration of Dy-DTPA was increased sequentially, ultimately bringing the concentration to 12 mM, in order to cover the range of susceptibilities found with Gd-DTPA during bolus-injections in typical blood volume measurement protocols. We used Dy-DTPA instead of Gd-DTPA because of its dramatically reduced dipole-dipole relaxivity, which would confound the effect under study. Solutions were placed in 5-cm long, 1.0-cm inner diameter cylindrical tubes which were imaged perpendicular to the main magnetic field.

To reduce the diffusion coefficient of the solutions from their room temperature values (2.3–2.6 µm^2/ms) to a more physiological level (1.0–1.5 µm^2/ms), the samples were cooled to 4°C and placed in an insulated, styrofoam holder for imaging. Typically, six to eight samples (different radii spheres, one sample without spheres, all at identical Dy-DTPA concentration) were imaged simultaneously. The temperature was monitored during imaging with a copper-constantan thermocouple in a spare tube. The temperature of this sample typically rose about 1°C in the 2 min required to acquire the images.

Imaging Experiments. We performed both spin echo and gradient echo imaging on a GE 1.5 T scanner, modified for single-shot imaging by Advanced NMR Systems (Wilmington, MA). To quantify transverse relaxation, we acquired 16 images with increasing TE, starting with $TE = 26$, and increasing in steps of 30, 15, 10, or 5 ms depending on the T_2 of the mixture. The repetition time, TR, was 6 s; slice thickness was 5 mm. Single-shot instant images (128 $\times$ 64 matrix, 3.1 mm $\times$ 3.1 mm in-plane resolution) were acquired, and reconstructed with a 2D Hamming window to reduce ringing and increase SNR of the individual measurements.

For gradient echo imaging, to minimize the contributions due to external magnetic field inhomogeneity and the perturbations caused by each tube on its neighbors, we imaged the tubes several times, permuting the tubes within the styrofoam holder. Again, the TE was varied in steps of 15, 10, or 5 ms depending on the T_2^*. Other imaging parameters were the same as for the spin echoes.

After each image set, we added Dy-DTPA to the

samples, and re-cooled the samples to 4°C. After acquiring spin and gradient echo *TE* data sets at each Dy concentration ([Dy] ≈ 3, 6, 9, and 12 m*M*), the samples were allowed to warm to room temperature. We acquired a *TE* data set, and measured the diffusion coefficient of the microsphere-free aqueous solution (38), every 4°C.

Analysis

As with the Monte Carlo simulations, the T_2 was measured by linear least-squares fitting of log signal intensity versus echo time for each microsphere/Dy-DTPA combination. In order to isolate the component of relaxation due to the susceptibility difference between the spheres and the solution, we subtracted both the relaxivity due to the normal dipole-dipole mechanism (measured in distilled water), and that solely due to the surface effects on the spheres:

$$\Delta R2 = \{R2_{r,[Dy]} - R2_{r,0}\} - \{R2_{0,[Dy]} - R2_{0,0}\} \qquad [4]$$

where $R2_{r,[Dy]}$ is the measured $1/T_2$ for the solution of spheres of radius r with concentration [Dy]. The $r = 0$ case represents no microspheres, i.e., doped water. Thus, the first term in Eq. [4] removes relaxation enhancement produced by the spheres alone (surface relaxation and inherent susceptibility difference between polystyrene and water); the second term removes the intrinsic dipole-dipole relaxivity caused by the Dy-DTPA.

For gradient echo images, we used this analysis for each tube permutation, replacing $R2$ with $R2^*$ in Eq. [4]. To minimize the effects due to the intrinsic shim of the magnet, and the effect of the tubes on each other, we chose the smallest $\Delta R2^*$ observed for each tube.

For comparison with these spheres, we performed Monte Carlo simulations at each of the Dy-DTPA concentrations for each size microsphere. To duplicate the experimental conditions, we performed two simulations for each sphere, one with a $\Delta\chi$ for the polystyrene alone ($\Delta\chi = 1.0 \times 10^{-7}$), and one with a $\Delta\chi$ increased by the Dy-DTPA concentration ($\Delta\chi = 1.0 \times 10^{-7} + 4.8 \times 10^{-8}$[Dy], where [Dy] is the concentration of Dy-DTPA in m*M*. We measured these susceptibility constants directly using an imaging technique (39).) In analogy with Eq. [4], we subtracted the relaxivities measured with Dy-DTPA from those of the polystyrene alone.

RESULTS

Typical raw data extracted from the imaging experiments are shown in Fig. 1, in this case for [Dy] = 9.6 m*M*. We see that the contrast agent does cause some direct dipole-dipole relaxation ($r = 0$), and that maximum relaxation at this concentration is produced by 6.3-μm diameter spheres. Over the full range of Dy-DTPA concentration and sphere sizes, we found approximately monoexponential decay.

Comparison of Theory with Experiment: Spheres

Susceptibility Dependence. Figure 2 shows empirical spin echo $\Delta R2$ (using Eq. [4]) versus Dy concentration, for
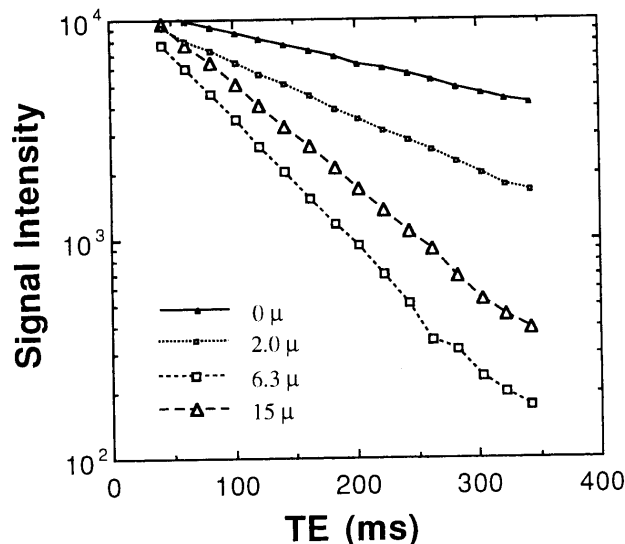

FIG. 1. Typical raw data from experiments at 4°C. Echo planar image intensity, *S*, is plotted against echo time, *TE*, for tubes containing 2% v/v microspheres, [Dy] = 6 m*M*. Each point represents a single Hahn echo image. Data show approximately linear dependence for log(*S*) versus *TE* for all size perturbers.
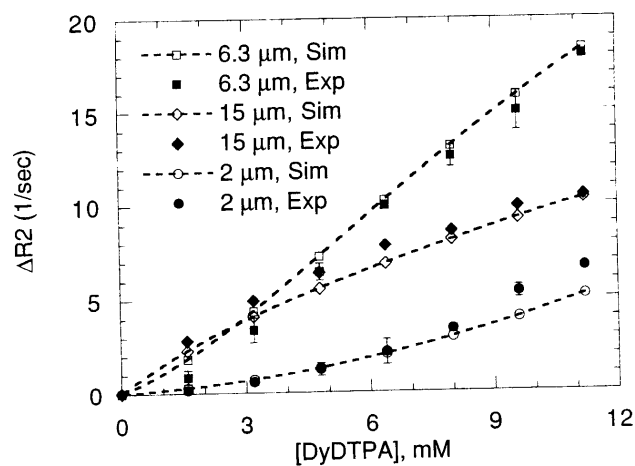

FIG. 2. Comparison of Monte Carlo calculations with experiment for 2 μ, 6.3 μ, and 15 μ diameter spheres in the range 0–12 m*M* Dy-DTPA, or $\Delta\chi = 0 - 0.6 \times 10^{-6}$, cgs, after removing the direct dipole-dipole and "un-doped" microsphere relaxation effects. The filled symbols are experimental data points, the open symbols are Monte Carlo data points.

three characteristic perturber diameters, 2, 6.3, and 15 μ, graphed with their Monte Carlo equivalents. For small particles, the susceptibility dependence is clearly superlinear, for large particles it appears sublinear, but for the 6.3 μ particles, $\Delta R2$ varies approximately linearly. There are no adjustable parameters in the Monte Carlo simulations, and thus the agreement between theory and experiment is striking.

Size Dependence. Figure 3 summarizes the size dependence of spin echo $\Delta R2$ for two concentrations, 3.2 and 9.6 m*M*. Both empirical measurements (solid) and Monte Carlo (open) results are shown. Agreement between
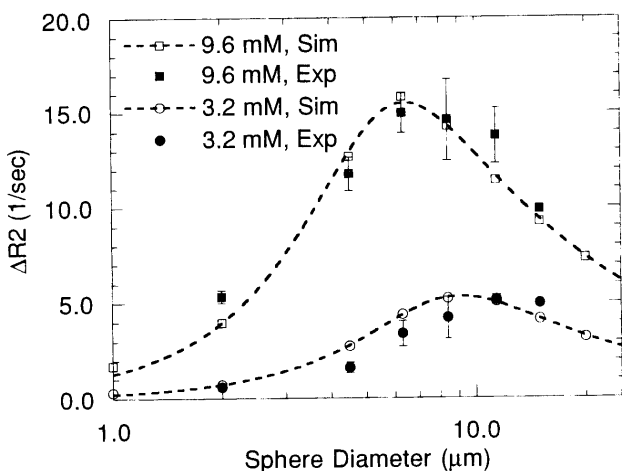
FIG. 3. Summary of size dependence of susceptibility-induced relaxation for two values of $\Delta\chi$. For both concentrations, we find a relaxivity peak between 5 and 10 µm. To the left of this peak, motional averaging reduces $\Delta R2$; to the right of this peak, the size of the gradient decreases with increasing particle size. Increasing concentration (increasing $\Delta\chi$) shifts the curves up and to the left. By tripling the concentration, we approximately triple the peak relaxation, and shift the curve over by approximately $\sqrt{3}$ in radius. The filled symbols are experimental data points, the open symbols are Monte Carlo data points. The error bars for the Monte Carlo simulations are smaller than the plot symbols.

theory and experiment is good throughout the range of the sizes measured. For both cases, the relaxation reaches a peak at 5 to 10 µ, though the $\Delta R2$-size curve shifts up and to the left as concentration of agent ($\Delta\chi$) increases.
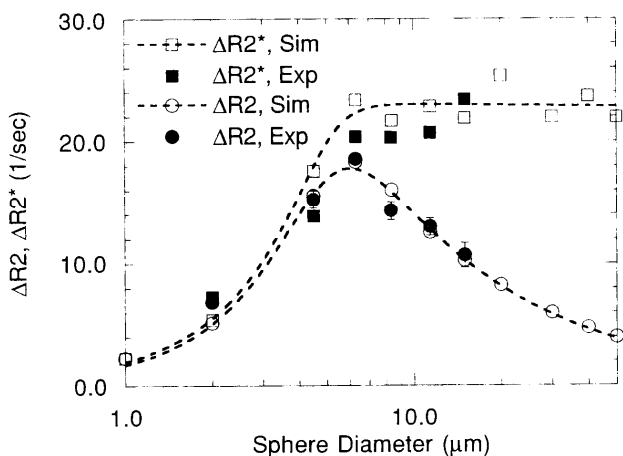

FIG. 4. Effective spin and gradient echo relaxivities ($\Delta R2$ and $\Delta R2^*$) measured at 11.2 m*M* Dy-DTPA at 4°C. For smaller particles, spin and gradient echo relaxivities are identical because proton diffusion is "fast" so that the 180° pulse does not refocus any effects that occured prior to it. To the right, gradient echo relaxivity is independent of perturber size because intravoxel dephasing dominates the signal loss; that is, diffusion is unimportant. The diffusion-independent regime for gradient echo begins at approximately perturber size corresponding to peak spin echo relaxivity. The filled symbols are experimental data points, the open symbols are Monte Carlo data points. The error bars for the Monte Carlo simulations are smaller than the plot symbols.

Figure 4 illustrates the size dependence for both spin and gradient echo from experiments and from simulation at the highest Dy-DTPA concentration. For the smallest perturbers, spin and gradient echo relaxivities are identical. Unlike $\Delta R2$, however, $\Delta R2^*$ does not fall off at larger perturber size, but remains flat in both experiment and simulation. Again, the agreement between theory and experiment is excellent.

Diffusion Coefficient Dependence. Figure 5 shows the measured diffusion coefficient, D, versus temperature, T, in the undoped, sphere-free tube. Over this range (2–20°C), D is quite linear with temperature, satisfying $D = 1.15 + 0.048\ T$ (µm²/ms).

Figure 6 shows $\Delta R2$ changes between the lowest (4°C) and highest (19°C) temperatures. From Fig. 6, we know these diffusion coefficients correspond to approximately 1.3 and 2.1 µm²/ms, respectively. For smaller particles, increasing D decreased $\Delta R2$, for the larger particles it increased $\Delta R2$, but for the medium sized particles, there was no diffusion dependence. From Fig. 4, we see that the region for which $\Delta R2$ is relatively independent of D corresponds to the peak relaxation.

Scaling Laws. As mentioned in the introduction, a disadvantage of the Monte Carlo methodology is that it is a calculational work-horse, but does not lend itself to broader phenomenological explanations. However, we can generalize the results of the individual Monte Carlo simulations by using simple scaling laws derivable from the Bloch-Torrey equation, which, in these cases, should yield relaxivity results equivalent to the Monte Carlo calculations, even though we cannot solve them analytically in this case. These scaling laws will tell us how to take one solution of the Monte Carlo simulation (for example, $\Delta R2$ as a function of particle size for a given diffusion coefficient and $\Delta\chi$) and scale it to different diffusion coefficients or perturbation strengths.
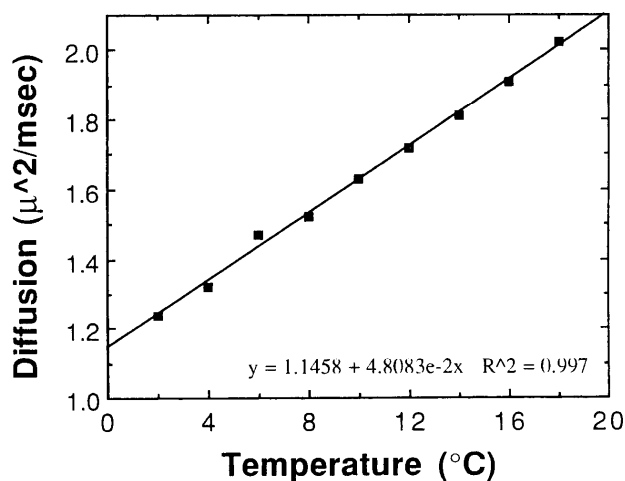
FIG. 5. Diffusion coefficient, D, in units of µm²/ms (10^{-5} cm²/s) measured by NMR as a function of temperature, T, in an un-doped, microsphere-free tube within the same styrofoam box as the microsphere laden tubes. Over this range of temperature, D varies linearly with temperature, and doubles between 0 and 25°C. By raising the temperature in the experiments, we monitored the effect of diffusion on the susceptibility-induced relaxation.

FIG. 6. Dependence of apparent spin echo relaxivity, $\Delta R2$, on temperature. Graph shows the difference between $\Delta R2$ measured at 19°C and 4°C as a function of size of the spheres. All measurements were performed on mixtures of 2% v/v microspheres at 11.2 mM Dy-DTPA. For small spheres (left side of graph), relaxation is *decreased* at higher temperature: more diffusion induces more averaging produces less effective relaxation. For large spheres (right 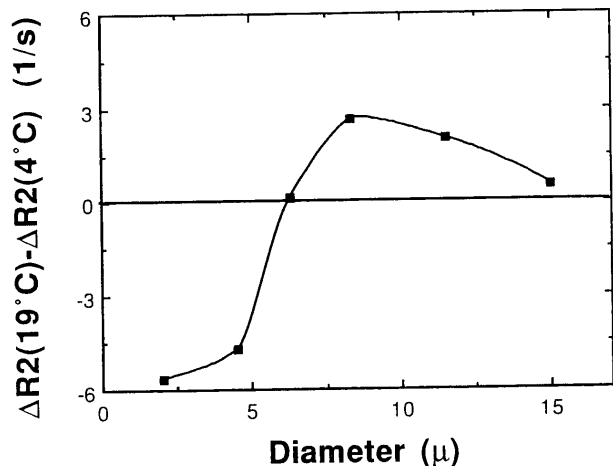side of graph), relaxation is *increased*. In the intermediate regime (for which relaxivity is locally maximum), there is little change with diffusion.

Ignoring other sources of T_2 relaxation, the transverse magnetization evolves as (26) :

$$\frac{dM(x, t)}{dt} = -i\omega(x)M(x, t) + D\nabla^2 M(x, t) \quad [5]$$

where $M(x, t)$ is the transverse magnetization, $M_x + i M_y$, D is the (isotropic) diffusion coefficient, and $\omega(x)$ is the spatially varying Larmor frequency. $M(x,t)$ is the solution for a given $\omega(x)$ produced by a specified volume fraction f of perturbers of size R, with peak frequency shift $\Delta\omega$ and a diffusion coefficient D. By integrating $M(x,t)$ over the object, we found (in our simulations and experiments) a monoexponentially decaying signal, which we characterized by the change in effective T_2 relaxivity, $\Delta R2(R, f,\Delta\omega,D)$. In this section, we consider the effect on $\Delta R2$ of changing the size of the perturbers and changing the absolute strength of the magnetic field perturbation while keeping the volume fraction fixed.

Scaling up the physical size of the perturbers by a factor λ is equivalent to changing to a new coordinate system, $y = \lambda x$. In this new coordinate system, $\omega_{new}(y) = \omega_{old}(x)$. If we change the coordinates of Eq. [5] to y, the Laplacian operator becomes $\nabla^2_x = \lambda^2\nabla^2_y$, and we therefore have, in this new system:

$$\frac{dM(y, t)}{dt} = -i\omega(y)M(y, t) + (\lambda^2 D)\nabla^2 M(y, t) \quad [6]$$

Thus, the evolution for perturbers that are λ times larger and diffusion coefficient were λ^2 times larger should be the same as the original system:

$$\Delta R2(R, f, \Delta\omega, D) = \Delta R2(\lambda R, f, \Delta\omega, \lambda^2 D) \quad [7]$$

A second implication of this relation is that we should expect D to enter any relaxivity expression only in the form (D/R^2).

In order to understand the effect of increasing the strength of the perturbation, we consider compressing time by a factor β (i.e., $t' = t/\beta$). This compression is equivalent to scaling up the perturbation by the same factor (i.e., $\omega(x)\rightarrow\beta\omega(x)$) with a higher diffusion coefficient:

$$\frac{dM(x, t')}{dt'} = -i(\beta\omega(x))M(x, t') + (\beta D)\nabla^2 M(x, t') \quad [8]$$

That is, in the new time frame the evolution would be the same if the diffusion coefficient were increased by a factor of β, or, using the scaling rule derived above, if the particles were decreased in size by a factor $\sqrt{\beta}$. If we quantify a monoexponential $\Delta R2$, this, too, has a factor of time in it ($d \ln S/dt$), and thus the time compression also increases the monoexponential decay constant by a factor of β. That is,

$$\Delta R2(R, f, \beta\Delta\omega, D) = \beta\Delta R2(\sqrt{\beta}R, f, \Delta\omega, D). \quad [9]$$

Even if decay is not monoexponential, we could write a similar scaling law for, say, the time required for the signal to drop to half its strength, and summarize all our expressions by this time. These two scaling laws are very general, and are independent of the fields that the perturbers cause, as long as these perturbers do not interact. Thus, these relations hold for any shape perturber and, we should expect, *in vivo*.

We can use these laws to help explain the concentration dependence of $\Delta R2$ seen with the simulations and confirmed with the microsphere experiments, as well as the linear dependence often seen *in vivo* (40). In Fig. 7, the solid line shows the prototypical results from the Monte Carlo simulations described above. The dotted line shows the results of doubling the strength of the perturbation; i.e., doubling $\Delta\chi$ in the simulations, or doubling the concentration of agent in the *in vitro* or *in vivo* experiments. Using Eq. [9] we should expect that, for the doubled perturbations, $\Delta R2\rightarrow 2 \ \Delta R2(\sqrt{2}R,f,\Delta\omega,D)$ and thus doubling the perturbation should produce twice the relaxivity that would have been obtained for perturbers that are $\sqrt{2}$ times larger. If there were no perturber size dependence for the relaxivity, $\Delta R2$ would thus be linear with concentration.

This relationship is shown schematically in Fig. 7 in (A) the diffusion-narrowed (i.e., where increasing diffusion decreases relaxivity) regime, and (B) in the maximum relaxivity regime. In the diffusion-narrowed (left) regime, the relaxivity should quadruple: one factor of two from the time compression, and a second factor of two because $\Delta R2 \sim R^2$ in this regime. (We expect this $R2$ dependence from Eq. [7]. In this narrowed regime, we expect $\Delta R2 \sim 1/D$ from general arguments (29), which must, by scaling, be an R^2/D dependence. That is, we expect quadratic dependence of relaxivity on concentration, as observed in Fig. 2, and consistent with previous calculations that were valid in this regime (29). In the large-sized (right) regime, the relaxivity will grow far more slowly because the shift to large perturbers reduces
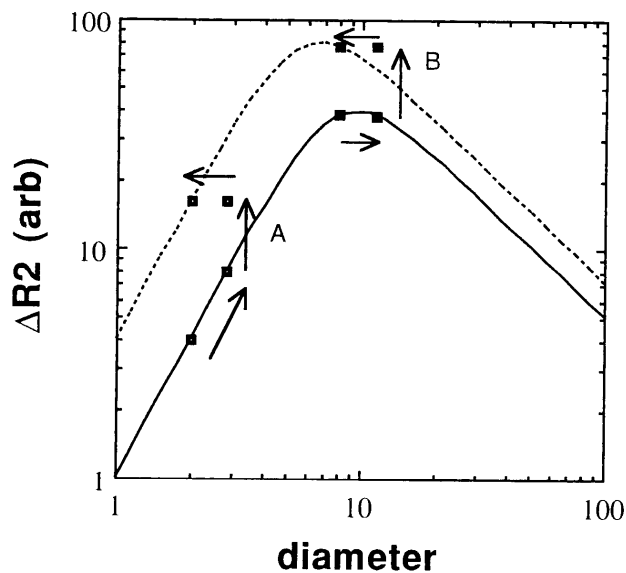
coff et al.

should
y in the

ing the
pressing
ssion is
he same
coeffi-

t') [8]

d be the
y a fac-
, if the
. If we
actor of
on also
y a fac-

[9]

write a
for the
all our
re very
he per-
iteract.
er and,

centra-
ns and
well as
Fig. 7,
om the
dotted
of the
or dou-
in vivo
for the
) and
ice the
urbers
er size
linear

. 7 in
diffu-
maxi-
l (left)
of two
of two
us R2
e, we
which
s, we
entra-
vious
n the
w far
duces

FIG. 7. Scaling laws and linearity at peak relaxivity. The solid and dashed lines represent typical $\Delta R2$ versus size curves at two different $\Delta \chi$, with the dashed line representing a doubling of $\Delta \chi$. The scaling laws suggest that the effective transverse relaxivity at twice the concentration should be twice the relaxivity for compartments that are $\sqrt{2}$ times larger. At point A, in the motionally narrowed regime, going from a 2 μ to 2.8 μ doubles $\Delta R2$ (first arrow). Doubling the resulting $\Delta R2$ (second arrow) produces a quadratic dependence with $\Delta \chi$ (third arrow). However, at peak relaxivity, point B, going from 8 μ to 11.3 μ hardly changes $\Delta R2$ (first arrow). Doubling this $\Delta R2$ (second arrow), then gives a simple doubling of $\Delta R2$ with $\Delta \chi$ (third arrow).

the time compression doubling. Thus, we expect sublinear $\Delta R2$-concentration curves, as, in fact, was seen in Fig. 3. Finally, in the intermediate regime, near the peak of the relaxivity curve, B on Fig. 4, for which there is little particle size dependence, we find linear behavior, because the shift to larger perturber size minimally affects relaxation.

As we see from Eq. [9], this linearity is very general, and depends only on the existence of some relatively broad peak. For example, for gradient echo experiments, for which there is a broad plateau for larger particles (see, for example, Fig. 4), we should observe linear dependence on concentration. In addition, because this linear dependence occurs at peak relaxivity for spin echo imaging, we should also expect to find linear behavior in a system that has a broad range of perturber sizes, such as is found *in vivo*. That is, as long as a reasonable fraction of the population of perturbers is near peak relaxivity in terms of their sizes, we will always observe linear behavior.

DISCUSSION

The excellent agreement between the Monte Carlo methods and the experimental results implies that the random walk model includes the most important processes for understanding transverse relaxation for the perturber sizes tested, despite the purely classical nature of the calculation.

Unlike other models (32, 41), our simulations and experiments specifically neglected water permeability, and thus focused on the extravascular effects of compartmentalized agent. In the brain, or for particulate iron oxide agents, we feel this model is appropriate. In particular, the lack of T_1 enhancement seen using Gd-DTPA in human brain studies and measurements of intravascular water lifetimes in normal, animal brain (~1 s (42, 43)) implies that extravascular exchange can play only a minor role in these cases. However, neglecting permeability is likely to confound the calculation *in vivo* when water permeability is high, such as in the heart and kidney. Studies that additionally incorporate water exchange (as well as the appropriate cylindrical geometry) into the Monte Carlo models so that balance between both paramagnetic relaxation and diffusion-mediated susceptibility effects can be determined are on-going.

The specific results of the simulations agree with previous theoretical calculations in the limits in which those calculations are valid. For example, the data on the left of Fig. 4 (motionally narrowed, $\Delta \omega \tau \ll 1$) agree generally with the predictions of Gillis and Koenig (29), showing quadratic increase with concentration. In addition, the shape of the curves is similar to those produced by Muller *et al.*(35) in Monte Carlo simulations for much smaller volume fractions of highly magnetized spheres. Comparing our results to Muller *et al.* (35), despite the widely different volume fractions (2 × 10⁻⁶ versus 2 × 10⁻²) and peak field shifts (3.4 × 10⁷ s⁻¹ versus 7 × 10² s⁻¹ for the peak of the 9.6 mM case in our Fig. 3) both systems show relaxivity peaks at approximately the same phase shift accrued by protons as they pass by the perturbers. For Muller's small magnetized spheres at their peak, we find this phase = $\delta \omega\, R^2/D = 2.7\pi$. For our much larger, but less magnetized, 6.3 μ particle we found, at peak, $\delta \omega\, R^2/D = 2.1\pi$. Our study confirms the difficulty of applying analytic approximations (such as ref. 44, 45, 31) without foreknowledge of the approximate regime in which the perturber system lies. This problem is especially acute as the most effective relaxivity never lies in the ranges for which approximations suffice, because it is precisely the region of compromise between the competing effects.

The right side of Fig. 4, specifically the $\Delta R2^*$ (gradient echo) curve, confirms Brown's result (46) $\Delta R2^* = (2\pi/3\sqrt{3})\, f \Delta\omega$, derived originally for oilwell logging. As shown in Fig. 4, at 11.2 mM Dy-DTPA, we found empirically and with the simulations that $\Delta R2^*$ asymptotes to 22 s⁻¹, compared with 25 s⁻¹ from Brown's formula. In addition, our data explain the disagreement between this formula and spin echo results: only in the motionally narrowed regime (where Brown's results do not apply) and at peak relaxivity are spin echo and gradient echo effects comparable. Above this peak relaxivity, for fixed $\Delta \chi$ and volume fraction, the larger the particle, the less useful an expression $\Delta R2^*$ is for predicting $\Delta R2$.

One possible confound in these simulations is the approximate nature of our "elimination" of the native susceptibility of the polystyrene spheres in the absence of added Dy-DTPA. We corrected for this susceptibility shift by subtracting the measured relaxivity of the spheres

alone rather than shifting the axis of the $\Delta R2$ versus [Dy] curve, Fig. 2. Our method of correction will artifactually reduce the quadratic curvature in the motionally narrowed case. Because the susceptibility of the spheres is quite low, and because we performed the same subtraction in the simulations, we believe the comparison between the results and the simulations remains valid, and the comparison with theory was made simpler by this subtraction.

A small error in our estimate of the susceptibility of these spheres may have led to the poorer agreement between theory and simulation in the lower concentration of Dy-DTPA in Fig. 3. Better agreement could be found by allowing the susceptibility of the polystyrene to vary, and finding the susceptibility that best fits the $\Delta R2$ versus [Dy] curves. However, we believed that the results were stronger with the small disagreement between experiment and a theory that had no free parameters.

While not explicitly demonstrated using the spherical case, we expect the general features of these results (i.e., strong compartment size dependence, wide range of diffusion dependence, linear and quadratic regimes) to be fairly independent of the exact shape of the compartment. As we demonstrated with the scaling laws, these specific solutions can also be generalized explicitly to explain why we observe linear behavior *in vivo*, despite the usual predictions of quadratic behavior for other limits. Although not exact, we can also use these results by analogy to address three issues: design and assessment of iron oxide contrast agents in the liver, assessing the possibility that capillary blood flow plays an important role in susceptibility contrast in the brain, and using the relaxivity-versus-size dependence to perform basic physiology experiments, such as understanding whether tissue blood volume changes are due to recruitment of marginally perfused vessels or dilatation of existing, perfused vessels.

The strong size dependence is likely to be of critical importance in optimizing and interpreting the results of iron-oxide contrast agents that are targeted to either hepatocytes or Kupffer cells in the liver. For example, measurements made using very small (<3 nm diameter) iron oxide particles (monocrystalline iron oxide nanoparticles, "MION" (47)) show quite different results *in vitro* and *in vivo* depending on whether the MION is directed to the hepatocytes or the Kupffer cells, and all show very different relaxivities in water solution than *in vivo*. For these particles, the T_2 relaxivity (per gram tissue or per milliliter water) have been found to be greatest in hepatocyte-directed agents, and smallest in water solution (48) Fig. 4 and the scaling laws can help us interpret these results.

Compared with free water, protons in the liver have a much lower effective diffusion coefficient. As a result, we would expect a shift to the right (because of the scaling dependence for R^2/D) on the relaxivity-size curve, Fig. 4, for particles measured *in vivo* compared with in water solution. The increased relaxivity in hepatocytes for spin echo imaging implies that the particles in water solution are in the motionally narrowed regime, so that decreases in diffusion create less averaging and thus

more effective relaxation. We would therefore predict that cooling an aqueous solution of these small particles would result in an increase in relaxation.

A more serious complication is the effect of particle size and distribution *in vivo*. While hepatocyte-directed agents tend to become uniformly distributed (compared with an average proton's random walk), the relative size and paucity of the Kupffer cells (about 2% by volume) implies that, in analogy to agent compartmentalized to the microvasculature in the brain, the Kupffer cell size may be the important compartment size, rather than the size of the particle or a particle-containing vesicle for RES-directed agents. "Concentration" of the agent, like diffusion, may produce either a decrease or increase in relaxivity, depending on where on Fig. 4 the native particle lies. Although it may be an oversimplification, we can interpret the reduction in efficacy of the RES-directed MION particles as shifting the relaxivity-size curve "too far" to the right; that is, beyond the peak relaxivity. This hypothesis can be tested by measuring $\Delta R2$ as a function of liver concentration. If, indeed, the RES-concentrated agent is to the right of peak relaxivity, then the relaxivity-concentration curve should be sublinear. In addition, because magnetic field distortions can be quite shape- and orientation-dependent (37), quantitatively accurate results would require appropriate modeling of the sequestering compartment.

As a second generalization, we predict the effect that movement of contrast agent within the vasculature could have during imaging. Hardy *et al.* (49) have shown the feasibility of using large magnetic particles within the vasculature to measure flow. In addition, White *et al.* (50), report dramatic decreases in $\Delta R2$ at death in animals that have a long-lived iron contrast agent in the blood, and attribute this drop to a blood velocity-induced mechanism. We believe our measurements argue against this interpretation of White's data, although it is consistent with Hardy's notion of flow-induced signal changes. This apparent paradox can be resolved by considering the relaxivity regime of the system. As demonstrated in Fig. 6, increased water mobility can either decrease (for small diameter), increase (for large diameter), or leave unaffected (for "peak" diameter) relaxivity, and that for the $\Delta\chi$ used in susceptibility contrast studies (White's work included), we are likely to be in the peak relaxivity domain. From the point of view of the proton, magnetic field variation caused by diffusion of the proton or by the perturber are, to first order, indistinguishable. By analogy, then, we expect that in the regime of minimum diffusion sensitivity, we should also expect minimal blood velocity sensitivity, and that the results of White *et al.* are more likely caused by a significant decrease in blood volume at death (51). A more complete test of this hypothesis is underway in a cylindrical capillary model that also includes motion of the blood compartments. The methods suggested by Hardy *et al.* use particles for which we are well *past* peak relaxivity on Fig. 6, so that motion of the perturbers will increase relaxivity, thus producing an exploitable flow-dependent effect.

A final use is to exploit the compartment size dependence of these effects to perform a basic biological meas-

urement: discriminating dilatation from recruitment in cerebral blood volume changes during physiological perturbation. In principle, at least, measurements made with an equilibrium susceptibility agent at peak relaxivity (i.e., at $\Delta\chi$ such that the $\Delta R2$ versus capillary diameter is at a maximum) should show the same, linear change in $\Delta R2$ whether blood volume increased because of a change in average capillary diameter (dilatation) or an increase in the number of perfused capillaries (recruitment). Such a measurement could be compared with the relative change with a much larger $\Delta\chi$ for which the peak relaxivity occurs at a vessel size that is smaller than the smallest capillary, e.g., 3 μ. In this case, recruitment should still change $\Delta R2$ linearly with blood volume, but dilatation would change $\Delta R2$ less than linearly, because the increase to larger capillary radii would decrease the effectiveness of the agent.

CONCLUSIONS

We have demonstrated that Monte Carlo modeling of microscopic susceptibility variation produces excellent predictions of apparent T_2 relaxation in simple phantoms. We have used these results to show that gradient echo images of tissue with agent compartmentalized in large enough compartments should show relatively little dependence on compartment size. Spin echo images, on the other hand, tend to show much greater dependence on geometry. In particular, we have demonstrated that it is reasonable that the T_2 effect should be linear with concentration over a wide and clinically useful range. In addition, the scaling rules present a logical framework with which to understand this apparently paradoxical behavior.

When combined with the simple scaling rules, these simulations provide a framework to understand apparent transverse relaxation caused by microscopic susceptibility variation. The understanding these models have produced is, we feel, both qualitative, in the sense that it helps explain the various regimes of behavior observed *in vivo*, and quantitative, because it predicts the magnitude of these relaxations accurately. We have used the results directly to predict diffusion and size effects in iron-oxide agents for the liver, by analogy to predict the absence of strong, velocity-dependent changes in brain contrast, and by extension, to suggest using the relaxivity-compartment size dependence to differentiate vasodilatation from recruitment of capillaries.

Ultimately, the mathematical modeling of complex biology relies on a series of approximations and assumptions. We believe Monte Carlo modeling, especially with the addition of generalizing rules, is a particularly attractive methodology for these models, because it provides the framework for including ever more complex features, and assessing the effects, if any, of these complexities.

REFERENCES

1. J. W. Belliveau, H. L. Kantor, I. L. Pykett, R. R. Rzedzian, P. Beaulieu, D. N. Kennedy, C. R. Fisel, T. J. Brady, B. R. Rosen, Real-time proton susceptibility-contrast imaging of hyper-capnia induced changes in cerebral physiology, *in* "Proc., SMRM, 7th Annual Meeting, San Francisco, 1988," p. 1.

2. M. E. Moseley, D. L. White, M. Wang, K. Roth, J. Dupon, R. C. Brasch, Determination of cerebral blood volume using an intravascular MRI contrast agent, *in* "Proc., ASNR, 27th Annual meeting, Orlando, FL, 1989," p. 19.

3. R. R. Edelman, H. P. Mattle, D. J. Atkinson, T. Hill, J. P. Finn, C. Mayman, M. Ronthal, H. M. Hoogewoud, J. Kleefield, Cerebral blood flow: assessment with dynamic contrast-enhanced T_2*-weighted MR imaging at 1.5 T. *Radiology* **176**, 211–220 (1990).

4. B. R. Rosen, J. W. Belliveau, H. J. Aronen, D. Kennedy, B. R. Buchbinder, A. Fischman, M. Gruber, J. Glas, R. M. Weisskoff, M. S. Cohen, F. H. Hochberg, T. J. Brady, Susceptibility contrast imaging of cerebral blood volume: human experience. *Magn. Reson. Med.* **22**, 293–299 (1991).

5. D. White, M. Wendland, K. Aicher, A. Tzika, M. Moseley, Susceptibility-enhanced echo-planar MRI: detection of regional cerebral ischemia in rat brain, *in* "Proc., SMRM, 9th Annual Meeting, New York, 1990," p. 57.

6. J. W. Belliveau, D. N. Kennedy, R. C. McKinstry, B. R. Buchbinder, R. M. Weisskoff, M. S. Cohen, J. M. Vevea, T. J. Brady, B. R. Rosen, Functional mapping of the human visual cortex using magnetic resonance imaging. *Science* **254**, 716–719 (1991).

7. R. Turner, A. Bizzi, D. Despres, J. Alger, G. DiChiro, Dynamic gradient-echo echo-planar imaging of deoxygenation in reversible global ischemia of cat brain, *in* "Proc., SMRM, 10th Annual Meeting, San Francisco, 1991," p. 1032.

8. J. Frahm, H. Bruhn, K. Merboldt, W. Hanicke, Dynamic MR imaging of human brain oxygenation during rest and photic stimulation. *J. Magn. Reson. Imaging* **2**, 501–505 (1992).

9. A. Blamire, S. Ogawa, K. Uğurbil, D. Rothman, G. McCarthy, J. Ellermann, F. Hyder, Z. Rattner, R. Shulman, Dynamic mapping of the human visual cortex by high-speed magnetic resonance imaging. *Proc. Natl. Acad. Sci. (USA)* **89**, 11069–11073 (1992).

10. R. Menon, S. Ogawa, S-G. Kim, J. Ellerman, H. Merkle, D. Tank, K. Uğurbil, Functional Brain Mapping Using Magnetic Resonance Imaging Signal Changes Accompanying Visual Stimulation. *Inv Rad* **27**(Suppl. 2), S47-S53 (1992).

11. K. Kwong, J. Belliveau, D. Chesler, I. E. Goldberg, R. M. Weisskoff, B. P. Poncelet, D. N. Kennedy, B. E. Hoppel, M. S. Cohen, R. Turner, H.-M. Cheng, T. J. Brady, B. R. Rosen, Dynamic Magnetic Resonance Imaging of Human Brain Activity During Primary Sensory Stimulation. *Proc. Natl. Acad. Sci. (USA)* **89**, 5675–5679 (1992).

12. P. Bandettini, E. Wong, R. Hinks, R. Tikofsky, J. Hyde, Time Course EPI of Human Brain Function during Task Activation. *Magn. Reson. Med.* **25**, 390–397 (1992).

13. G. N. Stewart, Researches on the circulation time in organs and on the influences which affect it. Parts I-III. *J. Physiol. (London)* **15**, 1 (1894).

14. R. W. Stow, P. S. Hetzel, An empirical formula for indicator-dilution curves as obtained in human beings. *J. Appl. Physiol.* **7**, 161–167 (1954).

15. K. L. Zierler, Theoretical basis of indicator-dilution methods for measuring flow and volume. *Circ. Res.* **10**, 393–407 (1962).

16. P. Meier, K. L. Zierler, On the Theory of the Indicator-Dilution Method for Measurement of Blood Flow and Volume. *J. Appl. Physiol.* **6**, 731–744 (1954).

17. N. A. Lassen, W. Perl, "Tracer Kinetic Methods in Medical Physiology," Raven Press, New York, 1979:

18. P. T. Fox, M. A. Mintun, M. E. Raichle, F. M. Miezin, J. M. Allman, D. C. Van Essen, Mapping human visual cortex

with positron emission tomography. *Nature* **323**, 806–809 (1986).

19. M. E. Phelps, J. C. Mazziotta, Positron emission tomography: Human brain function and biochemistry. *Science* **228**, 799–809 (1985).

20. D. Norman, L. Axel, W. H. Berninger, M. S. Edwards, C. E. Cann, R. W. Redington, L. Cox, Dynamic computed tomography of the brain: Techniques, data analysis, and applications. *AJR* **136**, 759–770 (1981).

21. L. Axel, Cerebral blood flow determination by rapid-sequence computed tomography: A theoretical analysis. *Radiology* **137**, 679–686 (1980).

22. G. T. Gobbel, C. E. Cann, J. R. Fike, Measurement of Regional Cerebral Blood Flow Using Ultrafast Computed Tomography: Theoretical Aspects. *Stroke* **22**, 768–771 (1991).

23. M. E. Raichle, Circulatory and Metabolic Correlates of Brain Function in Normal Humans, *in* Plum F ed. "Handbook of Physiology. The Nervous System V, Higher Functions of the Brain" (F. Plum, Ed.), pp. 643–674, Oxford University Press, New York, 1987.

24. N. A. Lassen, O. Henriksen, P. Sejrsen, Indicator methods for measurement of organ and tissue blood flow, *in* "Handbook of Physiology. The Cardiovascular System III" (J. T. Shepherd, F. M. Abboud, Eds.), pp. 21–63, American Physiological Society, Bethesda, MD, 1983.

25. E. L. Hahn, Spin Echoes. *Phys. Rev.* **80**, 580–594 (1950).

26. H. Torrey, Bloch equations with diffusion terms. *Phys. Rev.* **194**, 563–565 (1956).

27. B. Robertson, Spin-echo decay of spins diffusing in a bounded region. *Phys. Rev.* **151**, 273–277 (1966).

28. K. J. Packer, The effects of diffusion through locally inhomogenous magnetic fields on transverse nuclear spin relaxation in heterogenous systems. Proton transverse relaxation in striated muscle tissue. *J. Magn. Reson.* **9**, 438–443 (1973).

29. P. Gillis, S. H. Koenig, Transverse relaxation of solvent protons induced by magnetized spheres: application to ferritin, erythrocytes, and magnetite. *Magn. Reson. Med.* **5**, 323–345 (1987).

30. P. Bendel, Spin-echo attenuation by diffusion in nonuniform field gradients. *J. Magn. Reson.* **86**, 509–515 (1990).

31. S. Majumdar, J. C. Gore, Studies of diffusion in random fields produced by variations in susceptibility. *J. Magn. Reson.* **78**, 41–55 (1988).

32. W. Bauer, K. Schulten, Theory of contrast agents in magnetic resonance imaging: coupling of spin relaxation and transport. *Magn. Reson. Med.* **26**, 16–39 (1992).

33. C. R. Fisel, J. L. Ackerman, R. B. Buxton, L. Garrido, J. W. Belliveau, B. R. Rosen, T. J. Brady, MR contrast due to microscopically heterogeneous magnetic susceptibility: Numerical simulations and applications to cerebral physiology. *Magn. Reson. Med.* **17**, 336–347 (1933).

34. P. Hardy, R. M. Henkelman, Transverse Relaxation Rate Enhancement Induced by Diffusion of Spins through Inhomogeneous Fields. *Magn. Reson. Med.* **17**, 348–356 (1991).

35. R. N. Muller, P. Gillis, F. Moiny, A. Roch, Transverse Relaxivity of Particulate MRI Contrast Media: From Theories to Experiments. *Magn. Reson. Med.* **22**, 178–182 (1991).

36. H. Y. Carr, E. M. Purcell, Effects of diffusion on free precession in nuclear magnetic resonance experiments. *Phys. Rev.* **94**, 630–638 (1954).

37. S. C. K. Chu, Y. Xu, J. A. Balschi, C. S. Springer, Bulk magnetic susceptibility shifts in NMR studies of compartmentalized samples: Use of paramagnetic reagents. *Magn. Reson. Med.* **13**, 239–262 (1990).

38. R. McKinstry, R. Weisskoff, J. Belliveau, J. Vevea, J. Moore, K. Kwong, E. Halpern, B. Rosen, Ultrafast MR Imaging of Water Mobility: Animals of Altered Cerebral Perfusion. *J. Magn. Reson. Imaging* **2**, 337–384 (1992).

39. R. M. Weisskoff, S. Kiihne, MRI Susceptometry: Image-Based Measurement of Absolute Susceptibility of MR Contrast Agents and Human Blood. *Magn. Reson. Med.* **24**, 375–383 (1992).

40. R. Weisskoff, J. Belliveau, K. Kwong, B. Rosen, Functional MR Imaging of Capillary Hemodynamics, *in* "Magnetic Resonance Angiography: Concepts and Applications" (E. Potchen, Ed.), pp. 473–484, 1992.

41. R. P. Kennan, J. Zhong, J. C. Gore, On the relative importance of paramagnetic relaxation and diffusion mediated susceptibility losses in tissues, *in* "Proc., SMRM, 10th Annual Meeting, Napa, California, 1991," pp. 30–38.

42. M. S. Neuder, B. G. Jenkins, D. A. Chesler, J. B. Moore, R. B. Lauffer, B. R. Rosen, Estimation of the permeability of the blood brain barrier to water *in vivo* under normal and perturned conditions, *in* "Proc., SMRM, 10th Annual Meeting, San Francisco, 1991," p. 707.

43. M. Neuder, "A Study of Blood-Brain Barrier Permeability Variations *In Vivo* Using Magnetic Resonance Imaging," Ph.D. thesis, Massachusetts Institute of Technology, 1993.

44. R. Weisskoff, J. Dalcanton, R. Rzedzian, 40 Millisecond Instant Long Axis Heart Imagin, *in* "Proc., SMRM, 9th Annual Meeting New York, 1990," p. 123.

45. D. Chien, K. K. Kwong, D. R. Gress, F. S. Buonanno, R. B. Buxton, B. R. Rosen, MR diffusion imaging of cerebral infarction in humans. *AJNR* **13**, 1097–1102 (1992).

46. R. Brown, Some contrast agents in oilwell logging and in medical MRI. *Magn. Reson. Med.* **29**, 551–552 (1993).

47. R. Weissleder, A. Lee, B. Khaw, T. Shen, T. Brady, Antimyosin-labeled monocrystalline iron oxide allows detection of myocardial infarct: MR antibody imaging. *Radiology* **182**, 381–385 (1992).

48. T. Shibata, R. Weissleder, R. Schaffer, T. Shen, M. Papisov, T. Brady, Tissue relaxivities and detectability of monocrystalline iron oxides, *in* "Proc., SMRM, 11th Annual Meeting, Bertlin, 1992," p. 1416.

49. P. A. Hardy, M. J. Bronskill, M-J. Belanger, R. M. Henkelman, Use of magnetic particles for sensitizing MR images to blood flow. *J. Magn. Reson. Imaging* **1**, 431–440 (1991).

50. D. L. White, K. P. Aicher, A. A. Tzika, J. Kucharczyk, B. L. Engelstad, M. E. Moseley, Iron-dextran as a magnetic susceptibility contrast agent: flow-related contrast effects in T_2-weighted spin-echo MRI of normal rat and cat brain. *Magn. Reson. Med.* **24**, 14–28 (1992).

51. M. Tomita, Significance of cerebral blood volume, *in* "Cerebral Hypercapnia and Ischemia" (M. Tomita, T. Sawada, H. Naritomi, W. Heiss, Eds.), pp. 3–31, Elsevier Science Publishing Co, Inc., New York, 1988.